energies

MDPI

Article

Analysis of the Physical Properties of Hydrate Sediments Recovered from the Pearl River Mouth Basin in the South China Sea: Preliminary Investigation for Gas Hydrate Exploitation

Bin Wang [1], Peng Huo [1], Tingting Luo [1], Zhen Fan [1], Fanglan Liu [2], Bo Xiao [2], Mingjun Yang [1], Jiafei Zhao [1,*] and Yongchen Song [1,*]

1 Key Laboratory of Ocean Energy Utilization and Energy Conservation of Ministry of Education, Dalian University of Technology, Dalian 116024, China; lwwb1209@mail.dlut.edu.cn (B.W.); huopeng@mail.dlut.edu.cn (P.H.); ligongltt@mail.dlut.edu.cn (T.L.); fanzheng@mail.dlut.edu.cn (Z.F.); yangmj@dlut.edu.cn (M.Y.)

2 Guangzhou Marine Geological Survey, Guangzhou 510075, China; LVPF910@mail.dlut.edu.cn (F.L.); dlyanglei@mail.dlut.edu.cn (B.X.)

* Correspondences: jfzhao@dlut.edu.cn (J.Z.); songyc@dlut.edu.cn (Y.S.)

Academic Editor: Richard B. Coffin
Received: 16 January 2017; Accepted: 12 April 2017; Published: 13 April 2017

Abstract: Laboratory based research on the physical properties of gas hydrate hosting sediment matrix was carried out on the non-pressurized hydrate-bearing sediment samples from the Chinese Guangzhou Marine Geological Survey 2 (GMGS2) drilling expedition in the Pearl River Mouth (PRM) basin. Measurements of index properties, surface characteristics, and thermal and mechanical properties were performed on ten sediment cores. The grains were very fine with a mean grain size ranging from 7 to 11 μm throughout all intervals, which provide guidance for the option of a screen system. Based on X-ray Computed Tomography (CT) and SEM images, bioclasts, which could promote hydrate formation, were not found in the PRM basin. However, the flaky clay might be conducive to hydrate formation in pore spaces. The measured sediment thermal conductivities are relatively low compared to those measured at other mines, ranging from 1.3 to 1.45 W/(m·K). This suggests that thermal stimulation may not be a good option for gas production from hydrate-bearing sediments in the PRM basin, and depressurization could exacerbate the problems of gas hydrate reformation and/or ice generation. Therefore, the heat transfer problem needs to be considered when exploiting the natural gas hydrate resource within these areas. In addition, the results of testing the mechanical property indicate the stability of hydrate-bearing sediments decreases with hydrate dissociation, suggesting that a holistic approach should be considered when establishing a drilling platform. Both the heat-transfer characteristic and mechanical property provide the foundation for the establishment of a safe and efficient production technology for utilizing the hydrate resource.

Keywords: physical properties; hydrate-bearing sediment; Pearl River Mouth basin; production technology

1. Introduction

As a potential alternative strategic energy source and for the possible impact on the global climate, natural gas hydrates have aroused worldwide attention [1–5]. Gas hydrates are non-stoichiometric inclusion compounds made from water and light molecules, which are stable under high-pressure and low-temperature conditions [6–8]. Recently, a vast amount of gas hydrate has been naturally confirmed

in permafrost regions and beneath the sea floor by high-resolution seismic reflection data and pressure core testing [9–12]. The phase behavior of solid hydrates transformed into gas and water during the gas production process can significantly impact the stability of deposits, which leads to a risk of submarine landslide [13–15]. Thus, investigation on the physical properties of hydrate-bearing sediments has a huge importance on evaluating the possibility of potential mining operations on hydrate deposits.

In recent years, gas hydrate exploration and drilling work has been carried out in the South China Sea and the Qinghai-Tibet Plateau permafrost area, and the existence of gas hydrates has been confirmed [16–18]. China's second major expedition, the Chinese Guangzhou Marine Geological Survey 2 (GMGS2), was carried out in the eastern part of the Pearl River Mouth basin in 2013; the survey location was northeast of the Shenhu site, as is shown in Figure 1 [19,20]. By combining data from logging and core sampling, 9 of the 13 investigated sites including GMGS2-01, -04, -05, -07, -08, -09, -11, -12, and -16 were found to contain gas hydrates [21]. At sites GMGS2-07 and GMGS2-16, free gas was observed coming directly from boreholes. Extensive coring and pore-water analysis at site GMGS2-16 revealed evidence of a deep, coarse-grained aquifer about 200 m below the seafloor that might be supplying both free gas and fluids to the system. Liu et al. [20] conducted laboratory based studies on one of the sediment core samples recovered from the Pearl River Mouth Basin in the South China Sea, and determined information about the grain size of sediments, hydrate structure, hydration number, guest molecular compositions, and hydrate-bound gas origins. However, the current information about the physical properties of the sediments is still insufficient.

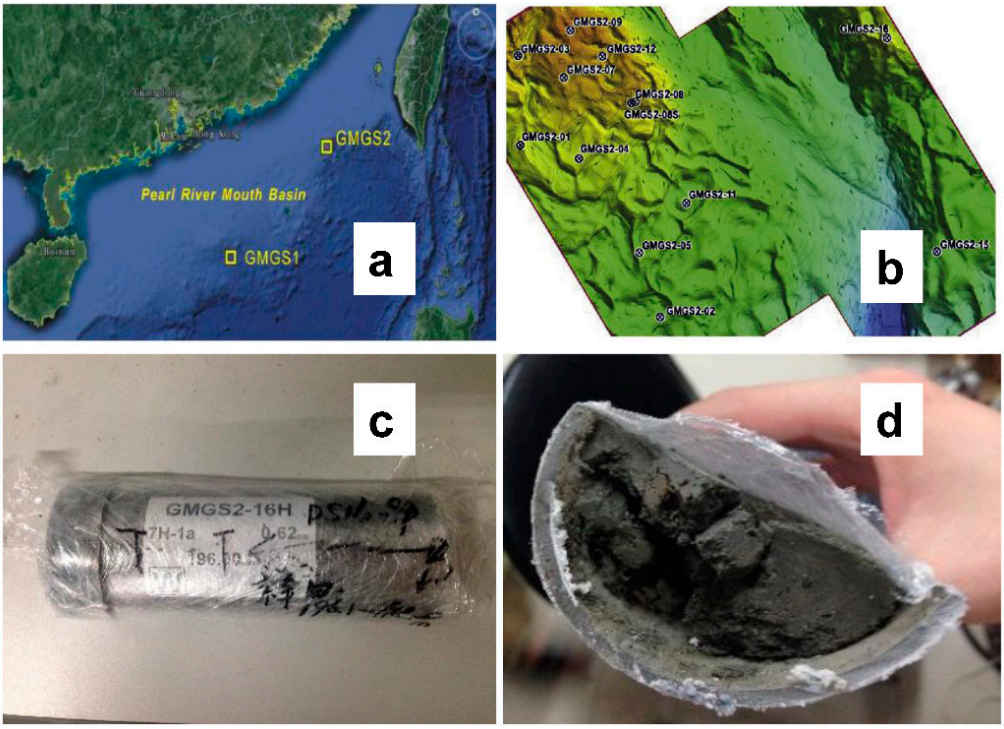

Figure 1. (**a**,**b**) Location of the Chinese Guangzhou Marine Geological Survey 2 (GMGS2) gas hydrate drilling exploration in the Pearl River Mouth basin in the South China Sea [19,20]; (**c**,**d**) photos of sediment core samples.

Knowing the physical properties of sediments can aid in the basic understanding of the gas hydrate occurrence rates and is important for the design and optimization of gas hydrate production technologies [22–24]. The establishment of safe and efficient production methods for utilization requires evaluating the production rate, well bore stability, and flow assurances [23]. Physical properties of the hydrate-hosting medium, such as particle size, thermal conduction characteristics, and mechanical properties, are important elements for these assessments [25,26]. Generally, particle size which

governs the sediment permeability plays an important role in affecting the occurring morphology and saturation of gas hydrate [27–29], and further affects water and gas production. Similarly, heat transfer from within the reservoir and from the over- and under-burden layers significantly influence the hydrate decomposition rate and the percentage of gas production [30,31]. Generally, the heat transfer capacity was controlled by the effective thermal conductivity of the surrounding sediments, which has been widely confirmed [32,33]. The mechanical property of hydrate-bearing sediments is a critical element for evaluating the stability of the hydrate-bearing sediments during gas production process. The hydrate dissociated into gas and water may increase the pore pressure and weaken the particles' interaction, further resulting in a variety of geological disasters including sediment deformation, production platform collapse, and submarine slope failure [34,35]. Such information about hydrate reservoirs can be approximated from regional geophysical investigations and then refined by direct geological and geochemical studies of cored sediments from a drilling well.

The gas hydrate sediment samples were de-pressurized and hermetically preserved at a temperature of 277.15 K while being transported and prepared for measurements in our laboratory. Thus, the hydrate decomposed completely when measuring the physical properties. The hydrate dissociation can impact chemical properties including gas content, crystalline structure, pore water activity, etc. However, intrinsic physical properties of the recovered sediments are little affected by the dissociation reaction. In this study, we determine the experimental results of sediment index properties, X-ray computed tomography scanning, surface characteristics, thermal transport properties, and mechanical properties of the hosting sediments, and we discuss some implications for production strategies. Nine samples belonging to GMGS2-16 (from 9 bmsf to 196 bmsf) and one sample belonging to GMGS2-09 were analyzed in our laboratory (these samples were numbered DS16-1 through DS16-9 and DS09-1, respectively). Data on the physical properties of these samples could aid in the analysis of corresponding field data and advance our understanding of hydrate occurrence and reservoir characteristics, further providing basic data for the design of drilling wells and the optimization of production technology.

2. Methods and Results

2.1. Index Properties

2.1.1. Specific Gravity

The specific gravity of the sediments was obtained with a pycnometer. The measured specific gravity values ranged from G_S = 2.708–2.841, and deceased with increasing depth, with the exception of sample DS16-6 from 81.45 to 81.53 mbsf (shown in Table 1). Previously reported values for this region could not be found for comparison; reference values are G_S = 2.26–2.37 for diatoms and G_S = 2.65 for kaolinite.

Table 1. Index properties of sediments.

Core Number	Interval and Length (mbsf)	Water Content (%)	Specific Gravity, Gs	Liquid Limit, WL (%)	Plastic Limit, Wp (%)
DS16-1	9.62–9.78	31.57	2.841	45.77	20.35
DS16-2	12.73–12.89	35.56	2.754	55.69	27.26
DS16-3	15.00–15.16	42.93	2.726	-	-
DS16-4	30.88–31.04	35.63	2.722	-	-
DS16-5	42.50–42.66	31.89	2.719	-	-
DS16-6	81.45–81.53	29.42	2.795	51.20	27.63
DS16-7	114.65–114.73	31.47	2.717	-	-
DS16-8	142.60–142.76	16.84	2.708	-	-
DS16-9	196.10–196.18	23.76	2.719	-	-
DS09-1	42.50–42.90	40.42	2.824	56.20	31.10

2.1.2. Water Content

The water content of the samples was obtained using an oven drying method and ranged from 16.84% to 42.93%. Our results show a general decreasing trend in water content with increasing depth, which means the compaction of the samples keeps pace with the sedimentation behavior; particle precipitation plays an important role in the formation process of sediments [36].

2.1.3. Atterberg Limits

The Atterberg liquid and plastic limits are defined as the water content values at the boundaries where the material transitions from liquid to plastic behavior and from plastic to brittle rheology, respectively; these limits are extensively used for identification, description, and classification of cohesive soils and as a basis for preliminary assessment of their mechanical properties. Factors such as specific surface, clay mineralogy, and fluid-dependent soil fabric formation influence the Atterberg limits of sediments [1,25,37]. The liquid and plastic limits of the samples were measured using the GB/T50123-1999 standard for soil tests. The liquid and plastic limits were taken to be the water content of the samples when a 76 g awl penetrated 17 and 2 mm into the sediment, respectively. Restricted by the total mass of the core samples, only four samples were analyzed in this part of the study. The liquid limit was measured to fall in the range W_L = 45.77–56.20%, and the plastic limit was W_P = 20.35–31.10%; both are shown in Table 1, and Figure 2 plots the plastic index (PI) corresponding to each liquid limit (W_L).

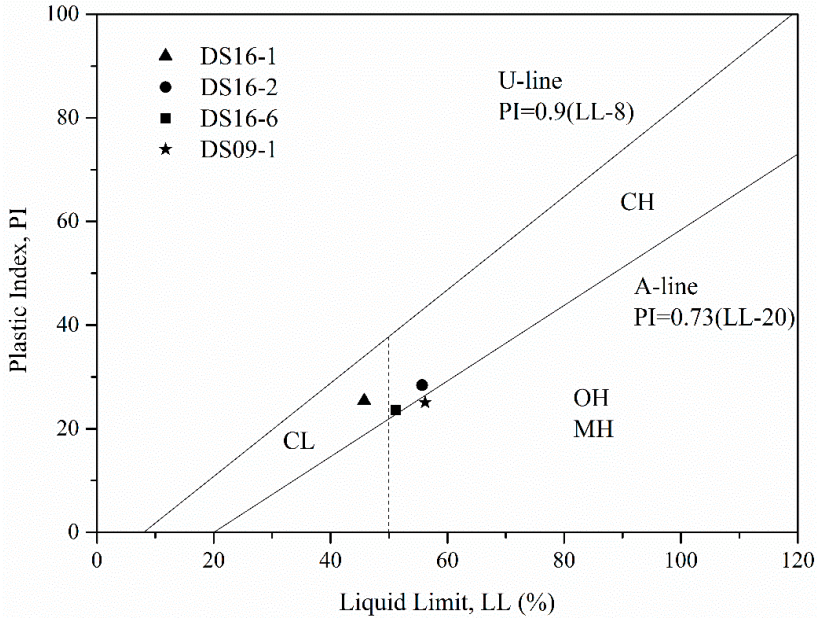

Figure 2. Liquid and plastic limits shown on the plasticity chart for the Pearl River Mouth basin sediments tested in this study.

In Figure 2, the PRM basin sediments fall within three zones based on the Unified Soil Classification System [38]. DS16-1 is classified as CL, i.e., "inorganic clays of medium plasticity", while DS16-2 and DS16-6 are both classified as CH, i.e., "inorganic clays of high plasticity". The DS09-1 sample, which is from a different site, is classified as either OH, i.e., "organic clay of medium to high plasticity" or MH, consistent with diatomaceous silty clay. These results indicate that the sediments in this region have a relatively low plastic index when compared with other regions [1,25]. This implies that the risk of collapse during gas production from hydrate sediments is higher in this region. Additionally, the results further suggest that collapse might be prevented if the water content can be monitored and kept below the plastic limit during hydrate exploitation processes.

2.1.4. Grain Size Distribution

Particle size is used to categorize sediments into different types (e.g., gravel, sand, silt) and plays an important role in gas hydrate occurrence morphology by determining the frequency of grain-displacing and pore-filling hydrates; particle size also influences the overall hydrate abundance by controlling the diffusion of methane gas [27]. An approximately 0.5 g sediment sample was dispersed in 1000 mL water with sodium hexmetaphosphate (0.5 mol/L) as a dispersant; the mixture was stirred for about one minute and then the particle size distribution was measured using a laser particle size analyzer. Each sample was measured three times consecutively, and the measurements were averaged. Table 2 shows the grain size analysis for PRM basin sediments as a function of depth. The mean grain size mostly ranges from 7 to 11 μm, generally decreasing from shallow to deep depths; however, the minimum mean grain size of 7.071 μm occurs at depths of 42.5–42.66 m. The samples from both the DS16 and DS09 sites show similar grain size distributions. A more detailed grain size distribution is shown in Figure 3. The grain sizes of the sediment samples range primarily from 0.3 to 150 μm; more than 95% of the grains are smaller than 63 μm, indicating that very fine grains dominate the sediment core samples. The grain composition is predominantly fine silt sand (4–63 μm, 67.043%) and clay (<4 μm, 28.74%), according to the category criteria of Shapard [39]. The results suggest that we should consider the sand plugging problem during gas hydrate exploitation because high fractions of fine particles can restrict the flow of gas and fluid.

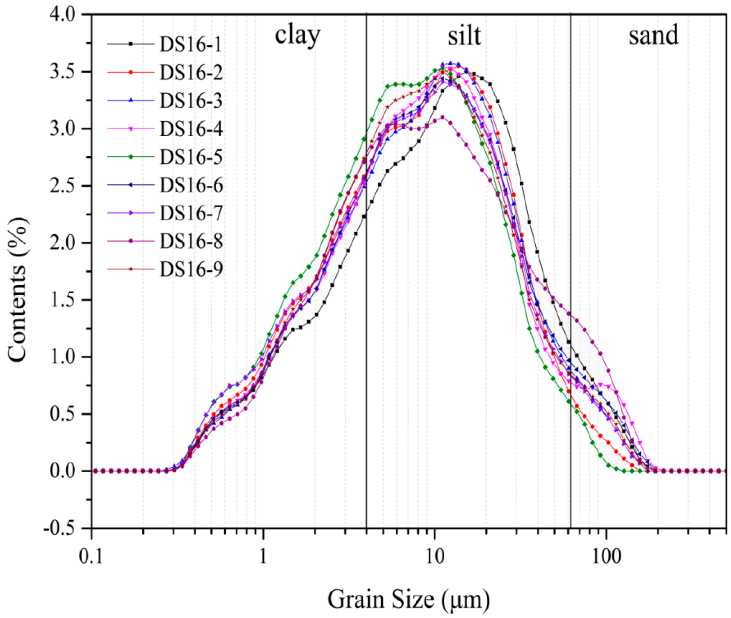

Figure 3. Particle size distributions of the hydrate-bearing sediments from the Pearl River Mouth basin.

Table 2. Particle size analyses at sites, where D_x is the grain diameter at x% of the cumulative grain size distribution.

Core Number	D_{50} (μm)	D_3 (μm)	D_{10} (μm)	D_{25} (μm)	D_{75} (μm)	D_{90} (μm)	D_{97} (μm)	D_{15}/D_{85}
DS16-1	10.69	0.739	1.620	4.123	23.22	43.75	81.44	1.613
DS16-2	8.560	0.714	1.468	3.426	18.47	32.65	57.63	1.620
DS16-3	9.132	0.750	1.564	3.676	19.57	37.17	72.91	1.605
DS16-4	8.905	0.743	1.561	3.689	19.36	39.76	94.80	1.596
DS16-5	7.071	0.656	1.337	3.016	15.30	27.62	49.73	1.594
DS16-6	8.926	0.749	1.577	3.672	19.87	40.80	83.79	1.615
DS16-7	8.283	0.658	1.368	3.297	18.51	35.93	72.12	1.640
DS16-8	8.950	0.830	1.679	3.647	22.46	51.48	91.87	1.684
DS16-9	8.271	0.761	1.572	3.518	18.23	36.34	75.00	1.602
DS09-1	7.156	0.671	1.376	3.091	15.67	30.21	66.46	1.591

2.1.5. Pore Characteristics

The porosity and pore size distribution of the recovered sediments were measured using mercury intrusion porosimetry (AUTOPORE IV 9500, Micromertics Instrument Corp., Norcross, GA, USA). An undisturbed sample produced by direct drying and a remolded sample produced through a drying-grinding-wetting-drying process are used for testing in this section. The relation curves of intrusion volume vs. mercury intrusion pressure are shown in Figure 4; the intrusion curves of both these two samples appeared as "S" type. The curve increases slowly at low mercury intrusion pressure, than increases faster as the pressure increases, indicating that a higher pressure refers to a larger porosity. In addition, we found the extrusion curve deviated from the intrusion curve as the pressure decreases, which means that some mercury still residues in the sediment pore. This is because the recovered sediments are vesicular structures with various shapes and different dimensions. The mercury firstly occupied the pore with higher pressure during the mercury intrusion process; however, the mercury extrusion process is far different as the continuous mercury line breaks and some mercury residues are in the pore. In conclusion, this variation is closely related to the pore structure. The final cumulative intrusion of the undisturbed sample is larger than that of the remolded sample, which means that the remolding process decreases the sediment porosity. The mercury intrusion porosimetry test curves of pore size distribution, cumulative volume, and cumulative surface area are shown in Figure 5. As shown, the incremental intrusion curve acted as a single peak distribution, and the pore size diameter of remolded sample mainly located in 0.1–1 μm, however, the pore size diameter of the undisturbed sample is slightly larger. As the figure shows, the cumulative pore area does not show obvious changes, even though the cumulative pore volume increases significantly.

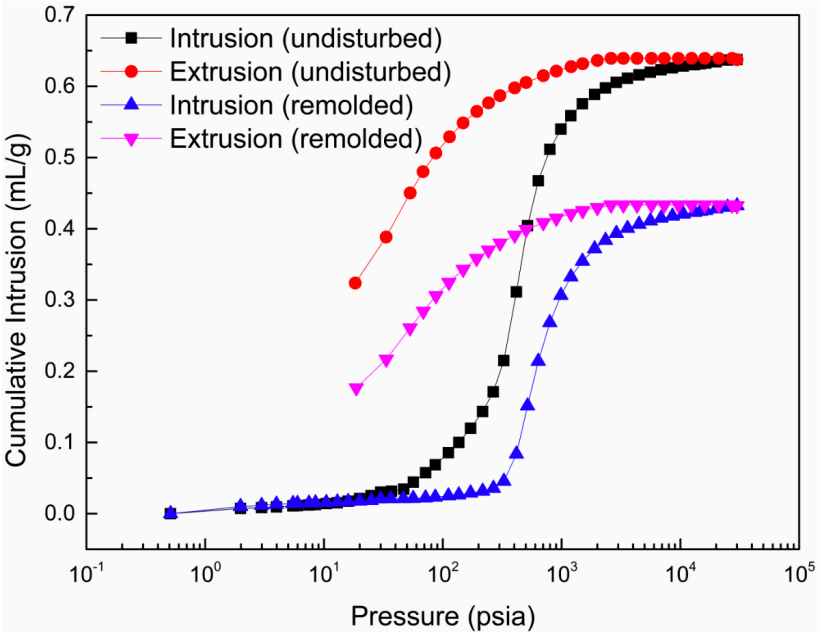

Figure 4. Relation between the volume of intrusion/extrusion and the pressure of mercury intrusion.

The results of the porosity test for undisturbed and remolded sediments are shown in Table 3. It is observed that structure reconstitution reduces the pore diameter and decreases the sediment porosity. The porosities of the undisturbed and remolded sediments are 67.73% and 57.98%, respectively. These values are relatively high. Mean volume pore diameters means the minimum diameters of pores when half of the total intrusion has taken place. When the sediment was remolded, the mean volume pore diameter falls to 120.2 nm from its original level of 195.4 nm.

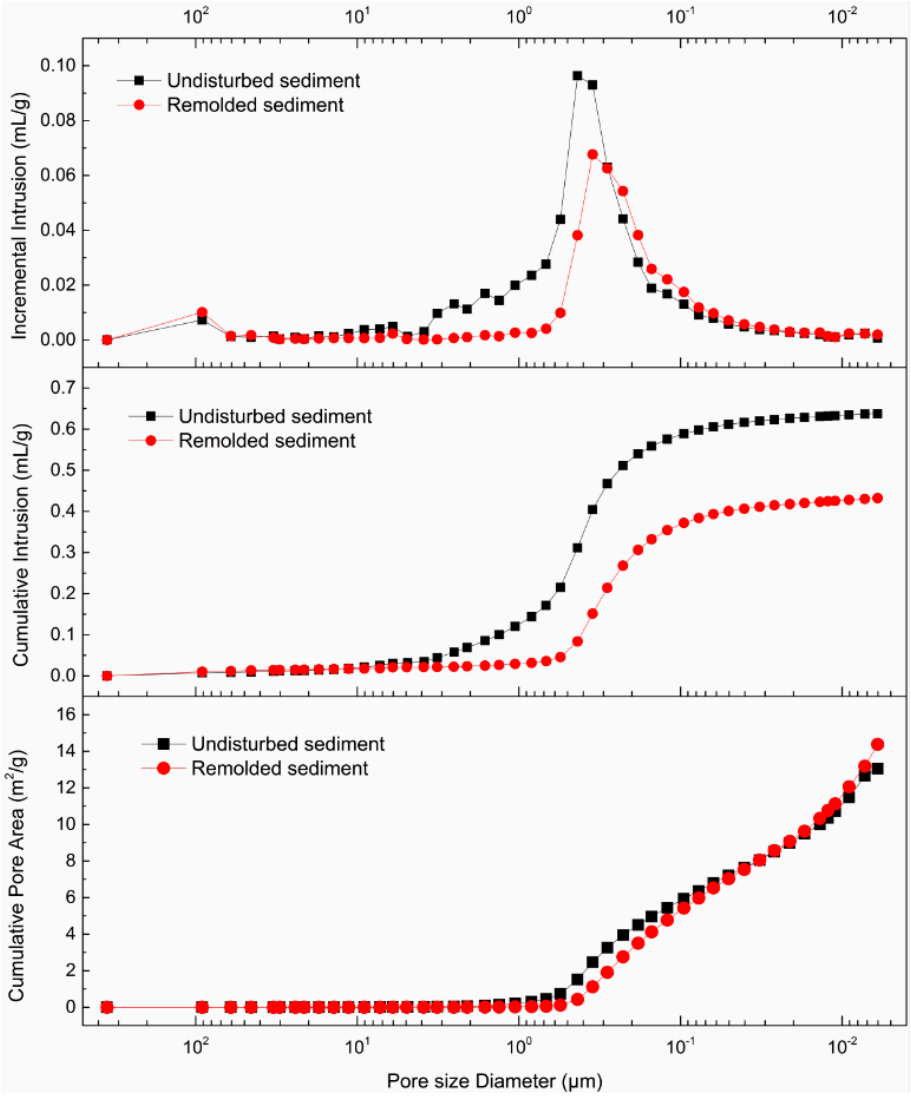

Figure 5. Mercury intrusion porosimetry test curves of pore size distribution, cumulative volume, and cumulative surface area.

Table 3. Mercury intrusion porosimetry analysis of the recovered sediments.

Samples	Median Volume Pore Diameter (nm)	Median Area Pore Diameter (nm)	Average Pore Diameter (nm)	Apparent (Skeletal) Density (g/mL)	Porosity (%)
Undisturbed sediment	426.1	71.3	195.4	3.29	67.73
Remolded sediment	281.8	47.0	120.2	3.19	57.98

2.2. Microstructure Observation

The frame structure of the recovered sediments was obtained by X-ray computed tomography (SMX-225CTX-SV, Shimadzu Co., Kyoto, Japan). The surface characteristics of air-dried powder sediments were measured using a Field Emission Scanning Electron Microscope (Nova NanoSEM 450, FEI Co., Hillsboro, OR, USA). The X-ray computed tomography and surface characteristics of the sediments are shown in Figures 6 and 7, respectively. The images reveal the major constituents of the sediments to be silt and clay minerals. Chen et al. [40] found that gas hydrate containing sediment layers in the Shenhu area were rich in calcareous nanofossils and foraminifers. Calcareous nanofossils

and foraminifers are small, but they are larger than most sediment grains in the Shenhu area; thus they probably aided gas hydrate formation and accumulation by increasing the sediment porosity [3]. Sediments rich in such bioclasts have not been found in the PRM basin. However, the flaky clay, present in the PRM basin, increases the contact area of the gas-water two-phase and may be conducive to hydrate formation in pore spaces; further study is needed for a full understanding of this process.

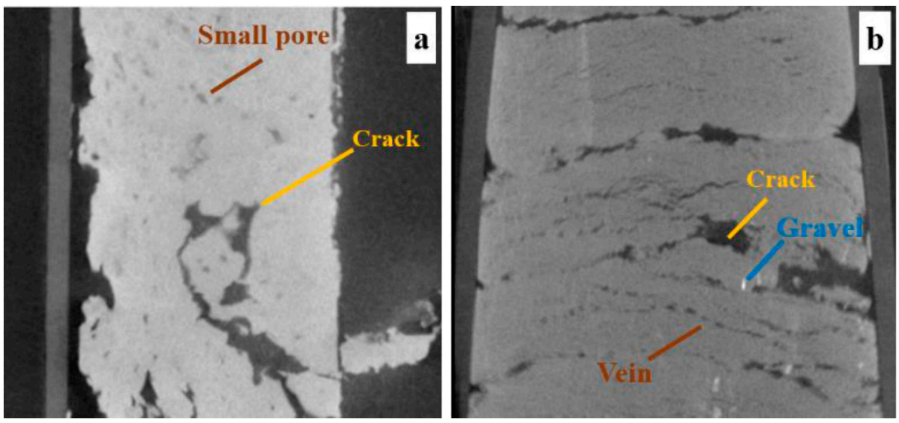

Figure 6. X-ray computed tomography of the DS16-3 sediment sample (**a**) and the DS16-6 sediment sample (**b**).

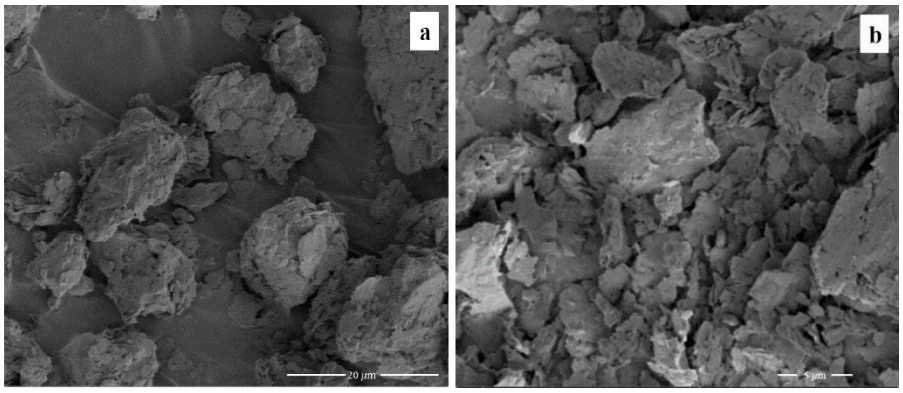

Figure 7. (**a**) SEM image of the DS16-3 sample at a magnification of 5000×; (**b**) SEM image of the DS16-6 sample at a magnification of 10,000×.

2.3. Thermal Transport Properties

The thermal conductivity of sediments is mostly governed by their bulk density and mineral compositions, with contributions from sediment fabrics. Thermal conduction within sediments involves the transport of heat between grains and the surrounding liquid; thermal conductivity is often reported for the mixture of sediment grains and pore fluids rather than for each component separately [26]. In this study, the thermal transport properties, including thermal conductivity, thermal diffusivity, and specific heat capacity, were measured simultaneously using a Hot Disk (TPS 2500S, Hot Disk AB Co., Gothenburg, Sweden) based on the Transient Plane Source Method [41]; these measured values will serve as useful references for the design of hydrate production technologies.

The thermal transport properties of the samples are given in Table 4. The measured thermal conductivities generally range from 1.3 to 1.45 W/(m·K), with the exception of DS16-8 and DS16-9, which have the relatively low values of 0.841 and 1.038 W/(m·K), respectively. These low conductivities are due to the samples' relatively low water content; this leads to the lower thermal conductivity because pore gases hinder heat transport. For comparison, we also measured the thermal conductivity

of water-saturated spherical glass sand (D_{50} = 0.4 mm), corundum, and white alundum; their conductivities are 0.53, 3.42, and 2.87 W/(m·K), respectively. Previous works report in-situ thermal conductivity measurements in the Ulleung basin ranging from 0.82 to 0.95 W/(m·K) [42], which is slightly lower compared to our PRM basin values.

Table 4. Thermal transport properties of the sediments.

Core Number	Thermal Conductivity (W/(m·K))	Thermal Diffusivity (mm^2/s)	Specific Heat (MJ/m^3K)
DS16-1	1.450	0.500	2.901
DS16-2	1.366	0.520	2.630
DS16-3	1.329	0.466	2.852
DS16-4	1.401	0.488	2.871
DS16-5	1.353	0.473	2.858
DS16-6	1.447	0.551	2.627
DS16-7	1.383	0.474	2.915
DS16-8	0.841	0.414	2.032
DS16-9	1.038	0.429	2.422
DS09-1	1.294	0.455	2.846

The high porosity of the sediments and the abundance of clay minerals are considered to be the main reason for their lower thermal conductivities. Thermal conductivity is also sensitive to the rate of gas production. Previous work reported that low thermal conductivity in sediments restricts heat transfer from the ambient region to the dissociation region; this limits the gas production rate due to the strong endothermic effect of the bulk decomposition stage [43]. The relatively low thermal conductivity in the PRM basin suggests that single thermal stimulation might not be a good option for gas hydrate production; additionally, depressurization could exacerbate ice generation or gas hydrate reformation problems by retarding heat flow from the surrounding areas to the cold gas hydrate dissociation front. Thus, heat transfer enhancement is an important aspect for the establishment of an efficient production method.

2.4. Mechanical Properties

The hydrate dissociated into gas and water may increase the pore pressure and weaken the particles' interaction, further resulting in a variety of geological disasters including sediment deformation, production platform collapse, and submarine slope failure. So, in order to establish a safe production method, studies on the mechanical properties of hydrate-bearing sediments both before and after the hydrate dissociation are necessary [35]. The mechanical properties of the samples were measured using a triaxial apparatus, which was detailed in our previous work [24]. Ice powder and sediment samples were used to remold the hydrate-bearing sediments in a pressure device at a controlled axial load of 30 kN. In this section, a series of experiments were conducted on the remolding of hydrate-bearing sediments by marine soil at temperatures of 8 °C under confining pressures of 2.5, 3.75, and 5 MPa; the strain rate was fixed at 1 %/min and the porosity was 40%.

2.4.1. Mechanical Properties of Remolding Methane Hydrate-Bearing Sediments by Marine Soil

In this study, the deviator stress is defined as the axial stress minus the confining pressure, and the axial strain is defined as the compressive displacement divided by the initial height of the specimen. Figure 8 shows the stress-strain curves and failure strength of the methane hydrate-bearing sediments under different confining pressures. All the curves in Figure 8a exhibit hyperbolic shapes and have three stages: the first elastic stage, the next elastic-plastic stage, and the end plastic stage. We also can observe the strain softening behavior of the methane hydrate-bearing sediments manufactured from the GMGS2 Gas Hydrate Drilling Expedition samples. The stress-strain curves of the hydrate-bearing sediments are significantly affected by the confining pressure; Figure 8b shows that the maximum deviator stress (failure strength) increases with increasing confining pressure. The failure strength of

hydrate-bearing sediments for confining pressures of 2.5 and 5 MPa are 0.83 and 1.53 MPa, respectively; Figure 8b shows that the relationship between failure strength and confining pressure is nearly linear, with a 90% increase between confining pressures of 2.5 and 5 MPa. The above results show that, while the GMGS2 samples show similar overall stress-strain properties, the failure strength is significantly affected by the confining pressure, especially in the low-pressure stage (lower than 5 MPa).

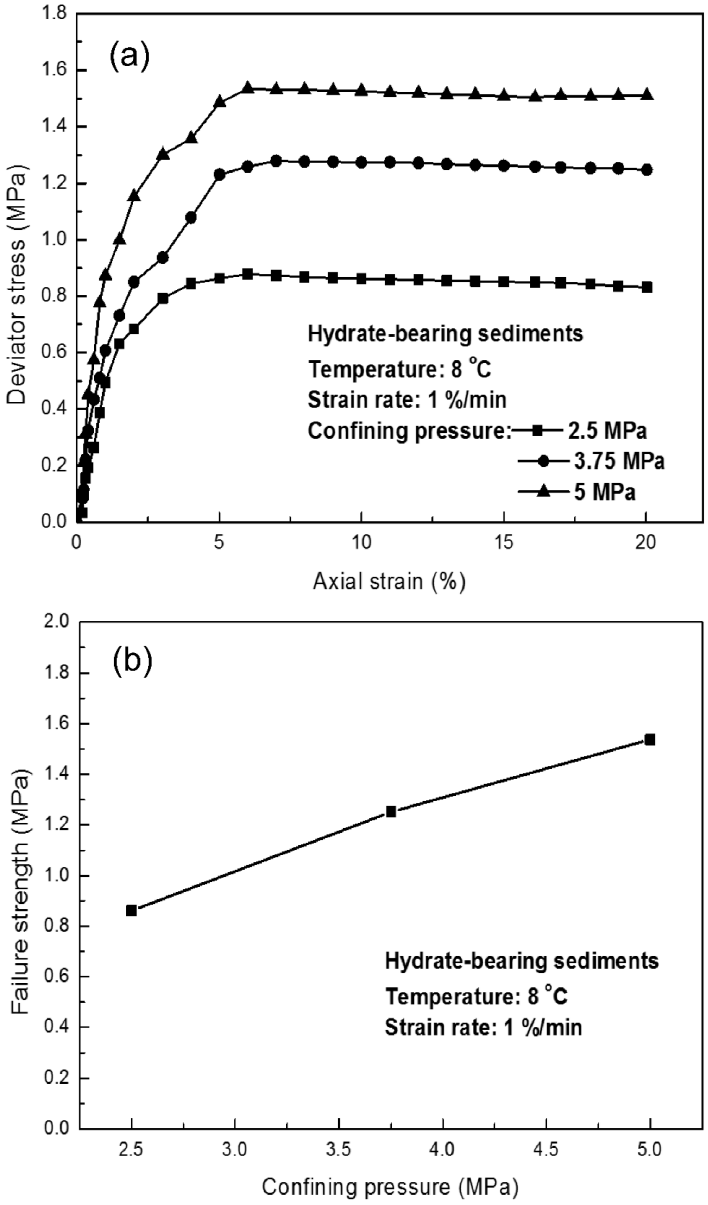

Figure 8. (**a**) Stress-strain curve and (**b**) failure strength of the artificial methane hydrate-bearing sediments manufactured from GMGS2 Gas Hydrate Drilling Expedition sediments.

2.4.2. Effect of Hydrate Dissociation on the Strength Property of the Methane Hydrate-Bearing Sediment

Figure 9 shows the stress-strain curves of methane hydrate-bearing sediments under different confining pressures after approximately two hours of hydrate dissociation. The data in Figure 9a exhibit the shape of a hyperbola, indicating that all specimens experienced elastic-plastic deformation. However, as shown in Figure 9b, the failure strength of all the hydrate-bearing sediments after 2 h of dissociation is lower than that before hydrate dissociation under different confining pressures.

The data accurately indicate that the strength of the sediments is broken by the dissociation of methane hydrate. The existence of methane gas in the pore spaces results in increased pore pressure, which, in turn, results in decreased sediment strength. Each successive hydrate dissociate event provides more methane gas, which further increases the pore pressure and further weakens the sediment strength.

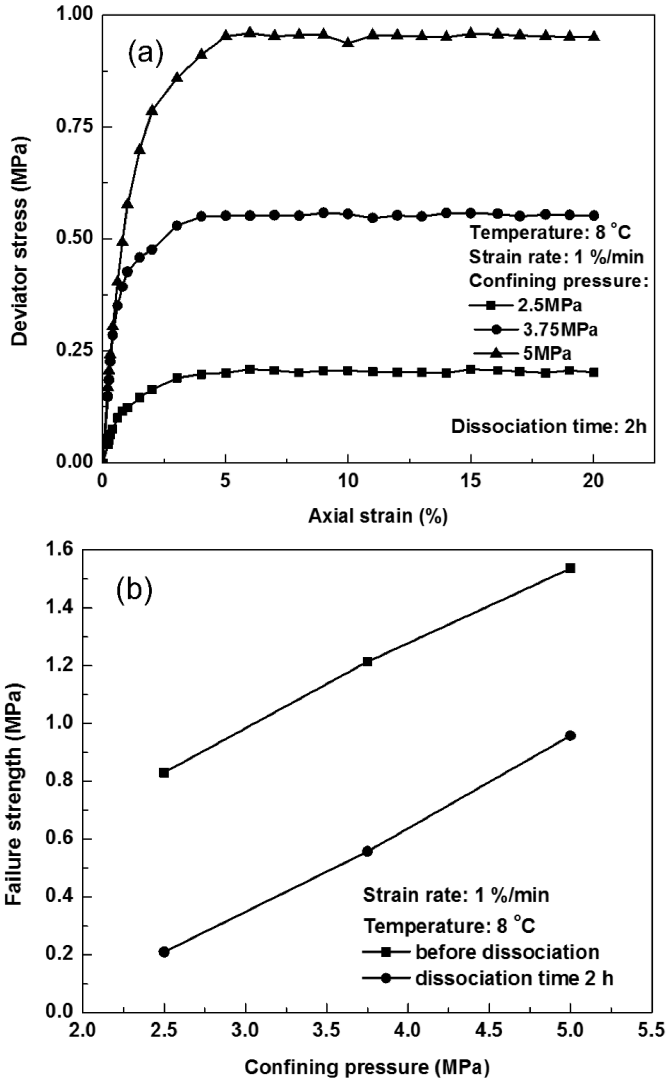

Figure 9. (**a**) Stress-strain curve of artificial methane hydrate-bearing sediments manufactured from GMGS2 Gas Hydrate Drilling Expedition sediments during the hydrate dissociation process under different confining pressures; (**b**) effect of hydrate dissociation on the failure strength of the same artificial methane hydrate-bearing sediments.

Previous research has shown that hydrate dissociation would lead to a significant decrease in the strength of hydrate-bearing sediments such as kaolin clay [24]. Based on those results as well as our results, under different confining pressures in the low-pressure stage (less than 5 MPa), the GMGS2 Gas Hydrate Drilling Expedition will experience lower failure strengths after hydrate dissociation. The dissociation of methane hydrate may cause the risk of deformation instability, production platform collapse, and submarine slope. Thus, we should take a holistic approach to evaluate the stability of the hydrate deposit when establishing a safe and efficient production platform.

3. Discussion

3.1. Grain Migration Behavior

The macro property of hydrate-bearing sediments during exploitation operations, which includes grain migration, fluid seepage, and reservoir deformation, is influenced by grain characteristics, fabric formation environments, and the resulting sediment fabrics [16]. The migration of grains could lead to serious problems in production. The mean grain size of sediments from the PRM basin is relatively finer than sediments in the Shenhu area where GMGS1 was conducted [3]. Thus when selecting the optimum screen system for gas production, grain migration concepts adapted from soil-mechanics could be useful. For preventing grain migration, the filter size should be smaller than at least four times the D_{85} of fine sediments, and in order to maintain suitable permeability and thus seepage force, the filter size should be larger than four times the D_{15} of coarse sediments [44].

According to Ref. [45], the potential particle migration issue can be determined using the grain size distribution, and the sediments could be considered as self-filtering when the ratio of D_{15}/D_{85} is less than four or five. The data for D_{15}/D_{85} in the PRM basin are detailed in Table 2 and plotted in Figure 10. The results shown the ratios are all less than four at both GMGS2-16 and -09. Using the criterion discussed above, all the analyzed sediments in the PRM basin are self-filtering. This feature will provide guidance for selecting the optimum screen system, which is associated with the design of the drilling well.

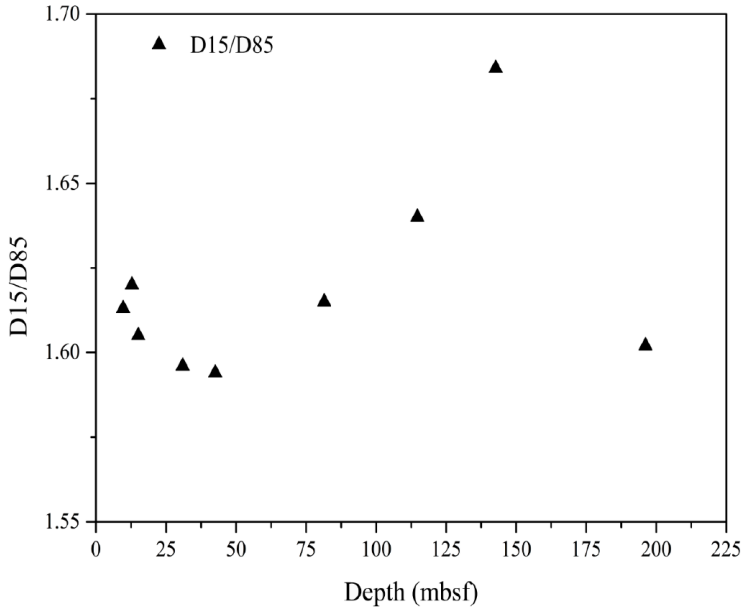

Figure 10. D_{15}/D_{85} of sediment samples as a function of depth.

3.2. Soil Types and Classification

The local effective stress and capillary pressure govern the hydrate growth morphology hosting in the sediments. A balance can be established at equilibrium, where the pressure in the hydrate phase (μ_h) is equal to the sum of the pressure in the water phase (μ_w) and the effective stress acting on the surface of the grain skeleton (σ'):

$$\mu_h = \mu_w + \sigma' \quad (1)$$

A dimensionless parameter which reflects the relative balance between hydrate-water capillarity and effective stress can be defined as:

$$\psi = \frac{\left(\frac{4\gamma_{hw}}{d_{th}}\right)}{\sigma'} = \frac{4\gamma_{hw}}{\left(\sqrt{2}-1\right)d_{10}\sigma'} \cong \frac{10\gamma_{hw}}{d_{10}\sigma'} \quad (2)$$

where the contact angle is assumed to be $\theta = 0°$, and the hydrate-water interfacial tension is $\gamma_{hw} = 0.032 \sim 0.039$ N/m [46]. The pore throat diameter (d_{th}) is determined by the fraction of fine sediment, taken to be ten percent of the finest grain size diameter here. The pore throat diameter is $d_{th} \cong \left(\sqrt{2}-1\right)d_{10}$ for simple cubic packing. The effective stress (σ') is calculated using the sediment depth and density of sediments as follows:

$$\sigma' = (\rho_s - \rho_w)gh \quad (3)$$

Figure 11 shows the ψ values at different depths. The results indicate that ψ decreases with increasing depth. This can be explained by the constant grain size distribution at different depths. Hydrates be more likely to occur in the form of grain displacement in shallow sediments when $\psi > 1$, as capillarity prevails and hydrates could displace particles more readily than they could invade pore throats [46], while hydrate growth would fill and invade existing pores rather than displace grains when $\psi < 1$, because of the high effective stress for equal grain sizes [46]. It can be seen that high effective stress with increasing depth promotes patchy hydrate distributions.

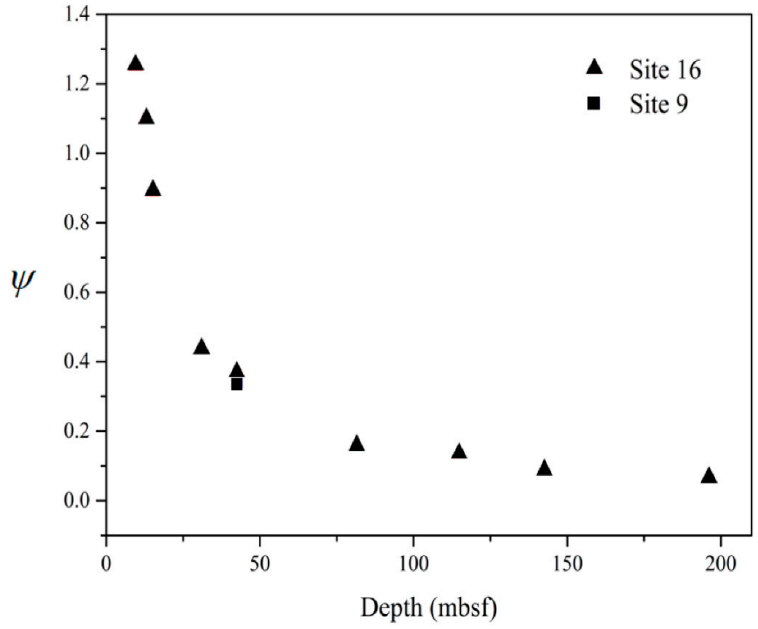

Figure 11. Values of ψ (Equation (2)) at different depths.

4. Conclusions

In summary, the index properties, X-ray computed tomography, and surface characteristics of recovered sediments were studied to investigate the hydrate occurrence morphology and reservoir characteristics. In addition, the heat-transfer characteristic and mechanical property of recovered sediments were studied to provide the foundation for the establishment of safe and efficient production methods for utilizing the hydrate resource. The petro-physical and geo-mechanical analyses on these measurements revealed the following:

(1) The mean grain size mostly ranges from 7 to 11 μm throughout all intervals. Additionally, we conclude that fine-grained layers are mostly self-filtering.

(2) From the computed tomography of X-ray and SEM, bioclasts have not been found, although the identified flaky clay increases the contact area of the gas-water two-phase; this may be conducive to hydrate formation in pore spaces.

(3) The measured thermal conductivities range from 1.3 to 1.45 W/(m·K), except for the GMGS2-16-8 and GMGS2-16-9 samples which have values of 0.841 and 1.038 W/(m·K), respectively. The relatively low thermal conductivity in the PRM basin suggests that thermal stimulation might not be a good option for gas production from hydrate-bearing sediments at the PRM basin, and depressurization could exacerbate the problem about ice generation and/or gas hydrate reformation. Heat transfer enhancement is an important aspect for the establishment of an efficient production method.

(4) The results of testing the mechanical properties indicate that Kaolin clay and sediments from the GMGS2 Gas Hydrate Drilling Expedition have the same stress-strain properties, and the stability of hydrate-bearing sediments decreases with hydrate dissociation, further causing the risk of sediment deformation, production platform collapse, and submarine slope.

Acknowledgments: This study has been supported by the National Science and Technology Major Project of China (Grant No. 2016ZX05028004-004), the Major Program of National Natural Science Foundation of China (Grant No. 51436003), and the Natural Science Foundation of China (Grant No. 51227005).

Author Contributions: Bin Wang and Zhen Fan analyzed the data and wrote the manuscript. Peng Huo and Tingting Luo performed the experiments. Fanglan Liu and Bo Xiao provided the hydrate-bearing cores. Jiafei Zhao conceived the original ideas. All authors discussed the results and commented on the manuscript. Mingjun Yang and Yongchen Song directed the overall project.

Conflicts of Interest: The authors declare no conflicts of interest.

References

1. Francisca, F.; Yun, T.S.; Ruppel, C.; Santamarina, J.C. Geophysical and geotechnical properties of near-seafloor sediments in the northern Gulf of Mexico gas hydrate province. *Earth Planet. Sci. Lett.* **2005**, *237*, 924–939. [CrossRef]
2. Han, H.; Wang, Y.; Li, X.S.; Yu, J.X.; Feng, J.C.; Zhang, Y. Experimental study on sediment deformation during methane hydrate decomposition in sandy and silty clay sediments with a novel experimental apparatus. *Fuel* **2016**, *182*, 446–453. [CrossRef]
3. Liu, C.L.; Ye, Y.G.; Meng, Q.G.; He, X.L.; Lu, H.L.; Zhang, J.; Liu, J.; Yang, S.X. The Characteristics of Gas Hydrates Recovered from Shenhu Area in the South China Sea. *Mar. Geol.* **2012**, *307*, 22–27. [CrossRef]
4. Koh, C.A.; Sum, A.K.; Sloan, E.D. State of the art: Natural gas hydrates as a natural resource. *J. Natl. Gas Sci. Eng.* **2012**, *8*, 132–138. [CrossRef]
5. Rossi, F.; Filipponi, M.; Castellani, B. Investigation on a novel reactor for gas hydrate production. *Appl. Energy* **2012**, *99*, 167–172. [CrossRef]
6. Sloan, E.D. Fundamental principles and applications of natural gas hydrates. *Nature* **2003**, *426*, 353–363. [CrossRef] [PubMed]
7. Castellani, B.; Rossi, F.; Filipponi, M.; Nicolini, A. Hydrate-based removal of carbon dioxide and hydrogen sulphide from biogas mixtures: Experimental investigation and energy evaluations. *Biomass Bioenergy* **2014**, *70*, 330–338. [CrossRef]
8. Castellani, B.; Rossetti, G.; Tupsakhare, S.; Rossi, F.; Nicolini, A.; Castaldi, M.J. Simulation of CO_2 storage and methane gas production from gas hydrates in a large scale laboratory reactor. *J. Pet. Sci. Eng.* **2016**, *147*, 515–527. [CrossRef]
9. Yun, T.S.; Fratta, D.; Santamarina, J.C. Hydrate-bearing sediments from the Krishna—Godavari Basin: Physical characterization, pressure core testing, and scaled production monitoring. *Energy Fuels* **2010**, *24*, 5972–5983. [CrossRef]
10. Shipley, T.H.; Houston, M.H.; Buffler, R.T.; Shaub, F.J.; McMillen, K.J.; Ladd, J.W.; Worzel, J.L. Seismic evidence for widespread possible gas hydrate horizons on continental slopes and rises. *AAPG Bull.* **1979**, *63*, 2204–2213.

11. Ecker, C.; Dvorkin, J.; Nur, A.M. Estimating the amount of gas hydrate and free gas from marine seismic data. *Geophysics* **2000**, *65*, 565–573. [CrossRef]
12. Collett, T.S.; Lee, M.W. Downhole well log characterization of gas hydrates in nature—A review. In Proceedings of the 7th International Conference on Gas Hydrates (ICGH 2011), Edinburgh, UK, 17–21 July 2011.
13. Waite, W.F.; Kneafsey, T.J.; Winters, W.J.; Mason, D.H. Physical property changes in hydrate-bearing sediment due to depressurization and subsequent repressurization. *J. Geophys. Res. Solid Earth* **2008**, *113*, B7. [CrossRef]
14. Nixon, M.F.; Grozic, J.L. Submarine slope failure due to gas hydrate dissociation: A preliminary. *Can. Geotech. J.* **2011**, *44*, 314–325. [CrossRef]
15. Yun, T.S.; Santamarina, J.C.; Ruppel, C. Mechanical properties of sand, silt, and clay containing tetrahydrofuran hydrate. *J. Geophys. Res. Solid Earth* **2007**, *112*, B4. [CrossRef]
16. Wu, Q.; Jiang, G. Assessing the permafrost temperature, thickness conditions favorable for the occurrence of gas hydrate in the Qinghai-Tibet Plateau. *Energy Convers. Manag.* **2010**, *51*, 783–787.
17. Zhu, Y.; Zhang, Y. Gas hydrates in the Qilian Mountain permafrost, Qinghai, Northwest China. *Acta Geol. Sin. Engl. Ed.* **2010**, *84*, 1–10. [CrossRef]
18. Wang, X.; Wu, S. Gas hydrate saturation from acoustic impedance and resistivity logs in the Shenhu area, South China Sea. *Mar. Pet. Geol.* **2011**, *28*, 1625–1633. [CrossRef]
19. Zhang, G.X.; Yang, S.X.; Zhang, M.; Liang, J.Q.; Lu, J.G.; Holland, M.; Schultheiss, P.; Team, G.S. GMGS2 expedition investigates rich and complex gas hydrate environment in the South China Sea. *Methane Hydrate Newsl.* **2014**, *14*, 1–5.
20. Liu, C.L.; Meng, Q.G.; He, X.L.; Li, C.F.; Ye, Y.G.; Zhang, G.X.; Liang, J.Q. Characterization of natural gas hydrate recovered from Pearl River Mouth basin in South China Sea. *Mar. Pet. Geol.* **2015**, *61*, 14–21. [CrossRef]
21. Wang, Y.; Feng, J.-C.; Li, X.-S.; Zhang, Y.; Li, G. Evaluation of Gas Production from Marine Hydrate Deposits at the GMGS2-Site 8, Pearl River Mouth Basin, South China Sea. *Energies* **2016**, *9*, 222. [CrossRef]
22. Dai, S.; Lee, C.; Carlos Santamarina, J. Formation history and physical properties of sediments from the Mount Elbert Gas Hydrate Stratigraphic Test Well, Alaska North Slope. *Mar. Pet. Geol.* **2011**, *28*, 427–438. [CrossRef]
23. Lee, J.Y.; Kim, G.Y.; Kang, N.K.; Yi, B.Y.; Jung, J.W.; Im, J.H.; Son, B.K.; Bahk, J.J.; Chun, J.H.; Ryu, B.J.; et al. Physical properties of sediments from the Ulleung Basin, East Sea: Results from Second Ulleung Basin Gas Hydrate Drilling Expedition, East Sea (Korea). *Mar. Pet. Geol.* **2013**, *47*, 43–55. [CrossRef]
24. Song, Y.C.; Zhu, Y.M.; Liu, W.G.; Zhao, J.F.; Li, Y.H.; Chen, Y.F.; Shen, Z.T.; Lu, Y.; Ji, C.M. Experimental research on the mechanical properties of methane hydrate-bearing sediments during hydrate dissociation. *Mar. Pet. Geol.* **2014**, *51*, 70–78. [CrossRef]
25. Lee, C.; Yun, T.S.; Lee, J.-S.; Bahk, J.J.; Santamarina, J.C. Geotechnical characterization of marine sediments in the Ulleung Basin, East Sea. *Eng. Geol.* **2011**, *117*, 151–158. [CrossRef]
26. Waite, W.F.; Santamarina, J.C.; Cortes, D.D.; Dugan, B.; Espinoza, D.N.; Germaine, J.; Jang, J.; Jung, J.W.; Kneafsey, T.J.; Shin, H.; et al. Physical Properties of Hydrate-Bearing Sediments. *Rev. Geophys.* **2009**, *47*, 38. [CrossRef]
27. Hailong, L.; Kawasaki, T.; Ukita, T.; Moudrakovski, I.; Fujii, T.; Noguchi, S.; Shimada, T.; Nakamizu, M.; Ripmeester, J.; Ratcliffe, C. Particle size effect on the saturation of methane hydrate in sediments—Constrained from experimental results. *Mar. Pet. Geol.* **2011**, *28*, 1801–1805.
28. Wang, J.Q.; Zhao, J.F.; Zhang, Y.; Wang, D.Y.; Li, Y.H.; Song, Y.C. Analysis of the effect of particle size on permeability in hydrate-bearing porous media using pore network models combined with CT. *Fuel* **2016**, *163*, 34–40. [CrossRef]
29. Oyama, H.; Konno, Y.; Suzuki, K.; Nagao, J. Depressurized dissociation of methane-hydrate-bearing natural cores with low permeability. *Chem. Eng. Sci.* **2012**, *68*, 595–605. [CrossRef]
30. Cheng, C.; Zhao, J.; Yang, M.; Liu, W.; Wang, B.; Song, Y. Evaluation of gas production from methane hydrate sediments with heat transfer from over-underburden layers. *Energy Fuels* **2015**, *29*, 1028–1039. [CrossRef]
31. Oyama, H.; Konno, Y.; Masuda, Y.; Narita, H. Dependence of depressurization-induced dissociation of methane hydrate bearing laboratory cores on heat transfer. *Energy Fuels* **2009**, *23*, 4995–5002. [CrossRef]

32. Pooladi-Darvish, M.; Hong, H. *Effect of Conductive and Convective Heat Flow on Gas Production from Natural Hydrates by Depressurization*; Kluwer Academic/Plenum Publishing Corporation: New York, NY, USA, 2004; pp. 43–65.
33. Zhao, J.; Wang, B.; Yang, L.; Cheng, C.; Song, Y. A novel apparatus for in situ measurement of thermal conductivity of hydrate-bearing sediments. *Rev. Sci. Instrum.* **2015**, *86*, 085110. [CrossRef] [PubMed]
34. Ning, F.; Yu, Y.; Kjelstrup, S.; Vlugt, T.J.; Glavatskiy, K. Mechanical properties of clathrate hydrates: Status and perspectives. *Energy Environ. Sci.* **2012**, *5*, 6779–6795. [CrossRef]
35. Li, Y.H.; Liu, W.G.; Zhu, Y.M.; Chen, Y.F.; Song, Y.C.; Li, Q.P. Mechanical behaviors of permafrost-associated methane hydrate-bearing sediments under different mining methods. *Appl. Energy* **2015**, *162*, 1627–1632. [CrossRef]
36. Flemings, P.B. Generation of overpressure and compaction—driven fluid flow in a Plio—Pleistocene growth—Faulted basin, Eugene Island 330, offshore Louisiana. *Basin Res.* **1998**, *10*, 177–196.
37. Yun, T.S.; Narsilio, G.A.; Carlos Santamarina, J. Physical characterization of core samples recovered from Gulf of Mexico. *Mar. Pet. Geol.* **2006**, *23*, 893–900. [CrossRef]
38. Mitchell, J.K.; Soga, K. *Fundamentals of Soil Behavior*; Wiley: New York, NY, USA, 1976.
39. Shepard, F.P.; Moore, D.G. Sedimentary environments differentiated by coarse-fraction studies. *AAPG Bull. Am. Assoc. Pet. Geol.* **1954**, *38*, 1792–1802.
40. Chen, F.; Su, X.; Zhou, Y.; Lu, H.F.; Liu, G.H.; Chen, Z.X.; Chen, C.Y. Variations in biogenic components of late Miocene-Holocene sediments from Shenhu Area in the northern South China Sea and their geological implication. *Mar. Geol. Quat. Geol.* **2009**, *29*, 1–8.
41. Gustafsson, S.; Karawacki, E.; Khan, M.N. Transient hot-strip method for simultaneously measuring thermal conductivity and thermal diffusivity of solids and fluids. *J. Phys. D Appl. Phys.* **1979**, *12*, 1411. [CrossRef]
42. Kim, Y.-G.; Lee, S.-M.; Matsubayashi, O. New heat flow measurements in the Ulleung Basin, East Sea (Sea of Japan): Relationship to local BSR depth, and implications for regional heat flow distribution. *Geo-Mar. Lett.* **2010**, *30*, 595–603. [CrossRef]
43. Zhao, J.F.; Zhu, Z.H.; Song, Y.C.; Liu, W.G.; Zhang, Y.; Wang, D.Y. Analyzing the process of gas production for natural gas hydrate using depressurization. *Appl. Energy* **2015**, *142*, 125–134. [CrossRef]
44. Terzaghi, K. *Soil Mechanics in Engineering Practice*; John Wiley & Sons: New York, NY, USA, 1996.
45. Jansen, R.B. *Advanced Dam Engineering for Design, Construction, and Rehabilitation*; Springer: Berlin/Heidelberg, Germany, 1988.
46. Dai, S.; Santamarina, J.C.; Waite, W.F.; Kneafsey, T.J. Hydrate morphology: Physical properties of sands with patchy hydrate saturation. *J. Geophys. Res. Solid Earth* **2012**, *117*, B11. [CrossRef]